NASA Technical Memorandum 100895
AIAA-88-2888

A Numerical Study of the Hot Gas Environment Around a STOVL Aircraft in Ground Proximity

Thomas J. VanOverbeke and James D. Holdeman
Lewis Research Center
Cleveland, Ohio

Prepared for the
24th Joint Propulsion Conference
cosponsored by the AIAA, ASME, SAE, and ASEE
Boston, Massachusetts, July 11-13, 1988

NASA

A NUMERICAL STUDY OF THE HOT GAS ENVIRONMENT AROUND A STOVL AIRCRAFT IN GROUND PROXIMITY

Thomas J. VanOverbeke* and James D. Holdeman†
National Aeronautics and Space Administration
Lewis Research Center
Cleveland, Ohio 44135

Abstract

The development of Short Take-off Vertical Landing (STOVL) aircraft has historically been an empirical- and experience-based endeavor In this study, a 3-D turbulent flow CFD code was used to calculate the hot gas environment around a STOVL aircraft operating in ground proximity Preliminary calculations are reported herein for a typical STOVL aircraft configuration to identify key features of the flow field, and to demonstrate and assess the capability of current 3-D CFD codes to calculate the temperature of the gases ingested at the engine inlet as a function of flow and geometric conditions.

Introduction

The development of Short Take-off Vertical Landing (STOVL) aircraft has historically been an empirical- and experience-based endeavor Several studies of various aircraft configurations and constituent flows have been published over the past two decades.[1-2] The availability and capability of current 3-D turbulent flow CFD codes[3-6] suggests that their application could provide a powerful new tool in analyzing the hot gas environment around a STOVL aircraft operating in ground proximity

In addition to the fluid dynamic phenomena associated with conventional external aerodynamics, STOVL configurations are affected by significant aeropropulsion interactions both in hover and in transition from hover to wing-borne flight.[7-10] In the STOVL flight regime, the aircraft typically has a low forward speed, is near the ground, and a large fraction of the lift is provided by vectored exhaust or lift jets. Because of the interactions between the airframe and the propulsion system flow, STOVL flow fields are very complex, and tend to vary considerably among possible aircraft configurations. Three-dimensional numerical simulations may provide insight into the flow physics to identify the key flow and geometric variables and guide analysis of new concepts. To date, CFD has not been systematically applied to this problem.

The objective of this study was to investigate the effects of flight speed and ground proximity on the hot gas environment around STOVL aircraft in order to identify key features of the flow field and demonstrate and assess the capability of current 3-D CFD codes to calculate the temperature of the gases ingested at the engine inlet for several flow and geometric conditions.

Description of the Flow Field

Ingestion of hot gases by the engine inlet has a deleterious effect in two ways: an average temperature rise results in a loss of engine thrust, and a temperature distortion may cause the engine to stall Engine exhaust gases may be ingested by either far- or near-field mechanisms A schematic of this flow field is shown in Fig. 1

In the far-field mechanisms, the exhaust gases from the lift jets impinge on the ground plane to form radial wall jets flowing outward in all directions from their impingement point. Those sections of the wall jet which flow forward in the direction of flight are stagnated by the headwind, and, due to their buoyancy, separate from the ground and rise to mix with the ambient air This fluid can then be drawn back into the engine inlet. The temperature of gases ingested at the engine inlet by this mechanism depends on the aircraft configuration, ground proximity, and flight speed.

*Aerospace Engineer, Internal Fluid Mechanics Division.
†Senior Research Engineer, Internal Fluid Mechanics Division, Member AIAA

Near-field ingestion arises with multiple jet configurations. In these, an upflow (fountain) is caused when outflowing wall jets from two adjacent lift jets meet. This upflow can then impinge on the underside of the fuselage. High inlet temperature levels can occur when these gases are allowed to flow along the bottom of the fuselage to the vicinity of the engine inlets and are ingested. Gases ingested by this near-field mechanism result in greater temperature distortion and tend to be hotter than those ingested via the far-field mechanism. Summaries of the previous work in this area are given in Refs. 1 and 2.

Numerical Model

Calculations were performed with a 3-D subsonic TEACH-type turbulent viscous flow code[11] on an AMDAHL MVS/XA computer This code solves the time-averaged Navier-Stokes or Reynolds equations. The k-ϵ turbulence model is used to provide closure. The governing equations are as follows:

Continuity

$$\frac{\partial}{\partial x}(\rho u) + \frac{\partial}{\partial y}(\rho v) + \frac{\partial}{\partial z}(\rho w) = 0$$

x-momentum

$$\frac{\partial(\rho uu)}{\partial x} + \frac{\partial(\rho uv)}{\partial y} + \frac{\partial(\rho uw)}{\partial z} = \rho g_x - \frac{\partial P}{\partial x} + \frac{\partial}{\partial x}\left(2\mu\frac{\partial u}{\partial x}\right) + \frac{\partial}{\partial y}\left[\mu\left(\frac{\partial u}{\partial y} + \frac{\partial v}{\partial x}\right)\right] + \frac{\partial}{\partial z}\left[\mu\left(\frac{\partial w}{\partial x} + \frac{\partial u}{\partial z}\right)\right]$$

y-momentum

$$\frac{\partial(\rho uv)}{\partial x} + \frac{\partial(\rho vv)}{\partial y} + \frac{\partial(\rho vw)}{\partial z} = \rho g_y - \frac{\partial P}{\partial y} + \frac{\partial}{\partial x}\left[\mu\left(\frac{\partial u}{\partial y} + \frac{\partial v}{\partial x}\right)\right] + \frac{\partial}{\partial y}\left(2\mu\frac{\partial v}{\partial y}\right) + \frac{\partial}{\partial z}\left[\mu\left(\frac{\partial w}{\partial y} + \frac{\partial v}{\partial z}\right)\right]$$

z-momentum

$$\frac{\partial(\rho uw)}{\partial x} + \frac{\partial(\rho vw)}{\partial y} + \frac{\partial(\rho ww)}{\partial z} = \rho g_z - \frac{\partial P}{\partial z} + \frac{\partial}{\partial x}\left[\mu\left(\frac{\partial w}{\partial x} + \frac{\partial u}{\partial z}\right)\right] + \frac{\partial}{\partial y}\left[\mu\left(\frac{\partial v}{\partial z} + \frac{\partial w}{\partial y}\right)\right] + \frac{\partial}{\partial z}\left(2\mu\frac{\partial w}{\partial z}\right)$$

Energy

$$\frac{\partial}{\partial x}(\rho uH) + \frac{\partial}{\partial y}(\rho vH) + \frac{\partial}{\partial z}(\rho wH) = \frac{\partial}{\partial x}\left(K\frac{\partial T}{\partial x}\right) + \frac{\partial}{\partial y}\left(K\frac{\partial T}{\partial y}\right) + \frac{\partial}{\partial z}\left(K\frac{\partial T}{\partial z}\right) + S$$

The calculations were done using air, with a constant specific heat, as the working fluid. Density is calculated using the equation of state.

All transport equations can be manipulated to the form

$$\frac{\partial}{\partial x}(\rho u\Phi) + \frac{\partial}{\partial y}(\rho v\Phi) + \frac{\partial}{\partial z}(\rho w\Phi) = \frac{\partial}{\partial x}\Gamma\frac{\partial\Phi}{\partial x} + \frac{\partial}{\partial y}\Gamma\frac{\partial\Phi}{\partial y} + \frac{\partial}{\partial z}\Gamma\frac{\partial\Phi}{\partial z} + S_\Phi$$

The source term S_Φ is linearized.

$$S_\Phi = S_p\Phi_p + S_u$$

Equations are discretized over small control volumes. A typical cell, with the variables noted, is shown in Fig. 2. Balancing the fluxes for variable Φ gives, for each control volume,

$$C_E\Phi_e - C_W\Phi_w + C_N\Phi_n - C_S\Phi_s + C_B\Phi_b - C_F\Phi_f = D_E(\Phi_E - \Phi_p) - D_W(\Phi_p - \Phi_W) + D_N(\Phi_N - \Phi_p) - D_S(\Phi_p - \Phi_S) + D_B(\Phi_B - \Phi_p) - D_F(\Phi_p - \Phi_F) + S_u + S_p\Phi_p$$

where, $C_E, C_W, \ldots$, are convention coefficients, $D_E, D_W, \ldots$, are diffusion coefficients, and S_u, is a source term. Introduction of weighing factors for convection and diffusion coefficients gives

$$A_p\Phi_p = A_N\Phi_N + A_S\Phi_S + A_E\Phi_E + A_W\Phi_W + A_B\Phi_B + A_F\Phi_F + S_u$$

where

$$A_p = A_N + A_S + A_W + A_E + A_B + A_F - S_p$$

A hybrid numerical differencing scheme was used in this study Hybrid differencing uses central differencing when the absolute value of the ratio of the convection coefficient

to the diffusion coefficient is less than two. At higher ratios, hybrid differencing reverts to first order upwind differencing.

In solving the transport equations the pressure field is needed. The SIMPLE (Semi-Implicit Method for Pressure-linked Equations) algorithm of Patankar[12] is used to provide the pressure field. In SIMPLE, the momentum equations are solved using the pressure field from the previous iteration. A pressure correction equation is then solved, and the momentum components are adjusted to more closely satisfy continuity

The calculation iterates for a specified number of cycles or until a chosen level of convergence is attained. Convergence is determined on the basis of a residual. The residual of one cell is defined as

$$R_\Phi = A_p\Phi_p - A_N\Phi_N - A_S\Phi_S - A_E\Phi_E - A_W\Phi_W - A_B\Phi_B - A_F\Phi_F - S_u$$

The residual is summed over the flow field and when this value divided by an appropriate nondimensionalizing number is less than a specified value the calculation is declared converged. The absolute value of each cell residual is used in the summation.

Three-dimensional numerical solutions using hybrid differencing schemes may contain a significant amount of false diffusion which affects numerical accuracy (e.g. Refs. 3 and 4). However, codes using k-ϵ turbulence models and hybrid differencing schemes have been shown to be a useful design tool in predicting trends and differences (see e.g. Refs. 4 and 6). Although more advanced schemes have been proposed to improve on the quantitative accuracy of current codes,[5,13-16] these require considerably greater computer memory, and/or have not been fully implemented and evaluated for 3-D flows.

Calculation Domain

Calculations were performed for a generic four-jet, side inlet STOVL aircraft configuration. Since the code used was developed for calculating internal flows, this model was immersed in a "wind tunnel," shown schematically in Fig. 3. A box-like shape was specified for the STOVL aircraft model because the code used has a Cartesian, rather than body-fitted, coordinate system. Since the flow field was symmetric about the aircraft centerline, only half of the flow field was calculated.

The wind tunnel was taken to be 4.5 ft high and 15 ft wide. The half width of the model fuselage was about 0.02 of the width of the tunnel. The sides of the square vertical lift nozzles were 0.4 times the half width of the fuselage. This dimension is referred to as D_j in the remainder of this paper. The distance between the centerlines of the forward and aft jets was $6(D_j)$. The side-to-side centerline separation for both forward and aft jets was $3.25(D_j)$. The height of the engine inlet duct was about $2.5(D_j)$. The engine inlet was $10(D_j)$ upstream from the centerlines of the forward nozzles, and the walls of the inlet duct were one grid cell thick. Sixteen grid cells were used for each nozzle. There were typically 12 x-z planes from the ground plane to the base of the fuselage, and another 12 across the engine inlet. For all configurations for which results are shown in this paper, there were 9 x-y planes from the aircraft centerline to the side of the fuselage. The entire calculation domain used 80 to 84 axial or x-gridpoints, 47 y-gridpoints, and 34 z-gridpoints. A nonuniform grid was used to concentrate cells in regions where large gradients in temperature and/or velocity were expected. A portion of a typical calculation grid is shown in Fig. 4. For cases with a weak headwind, additional gridpoints were needed upstream of the engine inlet so that the flow from the forward fountain did not reach the upstream boundary where inlet conditions were specified.

The forward part of the fuselage extended to the first axial plane of the modeled tunnel. Uniform temperature and velocity were specified around the fuselage at the upstream boundary. The freestream temperature was 70 °F and velocity was either 30 or 90.5 ft/sec. A uniform temperature of 1000 °F and velocity of 1000 ft/sec were specified for the vertical lift jets. This flow condition corresponds to a Mach number of 0.6, which was considered to be the upper limit of applicability of the code used as it did not include density correction terms due to rapidly changing pressure. (Including these terms in the code would allow calculation of transonic and supersonic flows.[17-19] Since several proposed STOVL aircraft configurations use underexpanded nozzles, accurate modeling of the actual flow conditions would require including these terms.)

The fuselage behind the jets extended to the tunnel exit for ease of calculation. A VonNeumann boundary condition was imposed at the downstream flow field exit. A symmetric boundary condition was used along the aircraft centerplane. A zero-velocity, adiabatic wall boundary condition was imposed at all sidewall boundaries. The computer code was modified to conserve mass between the tunnel calculation entrance and exit. Also, mass was conserved between the vertical lift jets and the aircraft engine inlet.

For large calculations, convergence within 5 percent (total residual divided by some appropriate nondimensionlizing number) is typical. However, as most of the changes in the flow field in these calculations occur in a very small portion of the calculation domain, lower values of the residual had to be specified. The mass averaged aircraft model inlet

temperature was also monitored. When this value showed signs of convergence, the calculation was terminated. Typically 2000 or more iterations were required to satisfy this criteria.

Results

The calculations performed in this study demonstrated the tractability of analyzing the STOVL hot gas environment with current CFD codes, and provide some insight into the effects of headwind and ground proximity on hot gas ingestion. The parameters varied were the distance from the exhaust lift jets to the ground plane, H/D_j, and the ratio of the forward speed of the aircraft (or strength of the headwind) to the exhaust jet velocity, U_∞/V_j. Although the latter is referred to as the headwind strength in this paper, it should be noted that a uniform velocity was specified at the upstream boundary of the calculation domain, rather than a nonuniform distribution as would be appropriate for an atmospheric boundary layer simulation.

Calculations were performed for two ratios of headwind-to-lift-jet velocity for each of two distances from the base of the aircraft fuselage to the ground. In the following sections, key features of the hot gas environment are identified in results from the calculation with $H/D_j = 4$ and $U_\infty/V_j = 0.03$. Following this, results are compared for cases with $H/D_j = 2$ and/or $U_\infty/V_j = 0.09$. For each case, ground plane temperature distributions beneath the aircraft are shown. In addition, temperature and velocity distributions in four horizontal (x-z) planes parallel to the ground, from near the ground to a plane through the bottom of the inlet, and temperature distributions in vertical (x-y) planes from the aircraft centerplane to just outboard from the fuselage are shown for each case. The contour and vector plots used in this report to display the numerical results are based on Graph3D.[20]

The conditions examined and the calculated inlet temperatures for them are given in Table 1. Values of the average dimensionless temperature difference ratio, defined as the average inlet temperature rise divided by the difference between the lift jet temperature (1000 °F) and the ambient temperature (70 °F), for these cases are given in Table 2. Table 3 gives the dimensionless inlet temperature distortion, defined as the difference between the maximum and minimum inlet temperatures divided by the difference between the jet and ambient temperatures.

Table 1. Jet, Ambient, and Inlet Temperatures for Cases Calculated[a]

U_∞/V_j	H/D_j	U_∞, kn	T_{avg}	T_{max}	T_{min}
0.03	4	17.8	187.7	388.2	109.8
.03	2	17.8	173.5	429.6	72.0
.09	4	53.6	145.1	469.9	61.6
.09	2	53.6	97.6	375.3	62.3

[a]At nozzle pressure ratio of 1.21, T_j = 1000; T_∞ = 70 (all temperatures are degrees F).

Table 2. Average Inlet Temperatures[a]

Distance from exhaust lift jets to ground plane, H/D_j	Ratio of forward speed of aircraft (or strength of headwind) to exhaust jet velocity, U_∞/V_j	
	0.03	0.09
4	0.13	0.08
2	11	.03

[a]$(T_{avg} - T_\infty)/(T_j - T_\infty)$

Table 3. Inlet Temperature Distortion[a]

Distance from exhaust lift jets to ground plane, H/D_j	Ratio of forward speed of aircraft (or strength of headwind) to exhaust jet velocity, U_∞/V_j	
	0.03	0.09
4	0.30	0.44
2	.38	.34

[a]$(T_{max} - T_{min})/(T_j - T_\infty)$

Features of the Flow Field

The CFD code used in this study predicts the key features of the flow field around a STOVL-type aircraft in ground proximity. As an illustration, velocities in the first x-z calculation plane above the ground are shown in Fig. 5, for the case where the base of the fuselage and the exhaust lift jets are four jet diameters above the ground ($H/D_j = 4$), and the ratio of the headwind velocity to the exhaust jet velocity, U_∞/V_j, is 0.03. The velocity vectors were plotted at different scales in two regions of the flow (differentiated by the shading in the figure) to show more detail. In this figure the aircraft is pointing toward the top of the figure, with the headwind flow from top to bottom. The flow field calculated on the right side of this figure has been duplicated with reflection to the left side to show the entire flow field which surrounds the aircraft.

The location where the jets impinge on the ground plane is evident in the figure. The flow is radially outward from each of these points. Where the radial outflow from adjacent jets impinge, the resultant flow is in a plane perpendicular to the line connecting the jet centerlines. The upflows perpendicular to the ground plane are generally referred to as fountains. Flow components along and perpendicular to the aircraft centerline midway between the forward and aft jets are also evident in Fig. 5.

The flow at about 45° to the fuselage centerline (clockwise from the top of Fig. 5) results from the combined effect of the forward jets and the diagonally opposite aft jets. The direction of the outer portion of this flow is affected by the strength of the headwind. At approximately 135°, flow from another diagonal alignment of lift jets is suggested. Because this flow is shielded from the headwind by the outflow from the fountain between the forward and aft jets, it is affected less by the strength of the headwind and diffuses into a larger portion of the flow field than the outflow in the forward quadrant. The dividing line between the flow from the forward and aft jets is indicated on the figure. This feature, and the strong forward flow along the aircraft centerline, is shown in the flow visualization results in Ref. 21.

Figure 6 shows the temperature contours in the x-z plane corresponding to the velocity field in Fig. 5. A contour plotting software package was used to smooth this distribution. The extent of the hot gas flow corresponds to strong outflow as shown by the velocity vectors. Particular features of note include the hot regions which result from the forward and rearward flow along the aircraft centerline, warm regions corresponding to the outflow at 45° and 135° to the aircraft centerline, and the hot gas outflow perpendicular to the aircraft centerline between the forward and aft jets.

In Fig. 7, near-field and far-field flows are shown by the velocity vectors in an x-y plane through the engine inlet and lift jets. The impingement of the jets on the ground plane and their subsequent redirection is evident in the figure. Part of the flow along the base of the fuselage is ingested into the inlet. This is near-field ingestion since the hot gases come directly from the fountain-lift jet area with limited mixing with ambient air.

The air ingested by the engine inlet may also include gases from the fountain-lift jet area which flow upstream of the engine inlet and are stagnated by the opposing headwind. This gas then flows downwind and may be ingested by the engine inlet. Ingestion by this mechanism is a far-field effect (sometimes referred to as ingestion by the ground-vortex flow). Figure 8 shows the temperature field corresponding to the velocity field in Fig. 7. The color code in this figure has been changed from that used in Fig. 6 to better emphasize features of the upstream boundary between ambient air and gases originating from the exhaust jets. Note the correspondence between the scalar and momentum fields, in particular the region of warm gas that extends forward of the inlet corresponding to the ground vortex flow.

Strength of the Headwind

$U_\infty/V_j = 0.03$ and 0.09 at $H/D_j = 4$. For the case with $U_\infty/V_j = 0.03$ and $H/D_j = 4$, the temperature contours in x-z planes parallel to the ground are shown in Fig. 9 for a plane near the ground (part (a)) to one cutting through the lower section of the inlet (part (d)). Part (b) is approximately halfway between the ground and the base of the aircraft fuelage, and part (c) is the plane just below the fuselage. In this (and subsequent) plan view sequences, the aircraft centerline is on the left side of the figure with the aircraft nose pointing up, and with the headwind from the top.

Only the region of the flow surrounding the lift jets on the right side of the aircraft centerline is shown in these figures since this is the region of primary interest in defining the hot gas environment. Also, these figures have not been smoothed to better show the expansion of the grid away from the aircraft.

The velocity vector plots in parts (a)-(d) of Fig. 10 correspond to the temperature field distributions in Fig. 9. These figures show that the outflow from the fountain between the two side lift jets is strongest near the ground. Above the ground plane the outward flow is relatively weak, some of it is almost immediately swept downstream once it rises around the fuselage (Figs. 9(d) and 10(d)). Flow to the rear of the fountain-lift jet system is relatively hot compared to the outflow from the fountain region between the forward and aft jets.

Temperature contours in x-y planes from the aircraft centerplane to just outboard from the fuselage are shown in Fig. 11. The headwind is from left to right in the figure. Part (a) corresponds to the first calculation plane by the aircraft centerplane; part (b) contains the first x-y plane of the engine inlet, part (c) contains the last x-y plane in the engine inlet duct and part (d) is the second calculation plane away from the side of the aircraft fuselage. Part (d) shows some of the outflow from the fountain area rising and being blown to the rear, as mentioned previously. Along the aircraft centerplane, flow is hottest toward the ground planes. The temperatures are also hotter between the fountain and aft lift jets than between the forward lift jets and fountain. The horizontal velocity vector diagram for this case in Fig. 10 shows flow coming into the region

forward of the fountain. The inlet temperatures are highest in the lower inside corner, consistent with the results reported in Ref 22

The average dimensionless inlet temperature rise for the case with $U_\infty/V_j = 0.03$ and $H/D_j = 4$ is 0.13; the maximum dimensionless temperature difference for this case is 0.30 (see Tables 2 and 3).

A stronger headwind velocity of $U_\infty/V_j = 0.09$ decreases the amount of hot gas ingestion. The average dimensionless inlet temperature rise drops to 0.08; however, the maximum dimensionless inlet temperature difference increases to 0.44. Figure 12 shows a color-coded temperature field near the ground plane for this case ($U_\infty/V_j = 0.09$, $H/D_j = 4$). This temperature distribution has been smoothed, and the calculated flow field is duplicated on the left side, as was done for Fig 6. The most obvious effects of the stronger headwind are the downwind sweep of the flow from the aircraft lift jets and the stagnation of the forward hot gas flow just upstream of the engine inlet

Temperature distributions for four x-z planes parallel to the ground are shown in Fig. 13. The corresponding velocity vector plots are shown in Fig 14 Hot gas from the lift jets does not penetrate nearly as far forward against the stronger headwind, and stagnation occurs just upstream of the engine inlet (which is at $x = 8$ in Fig. 14). The side flow from the fountain area in planes (b) and (d) is also greatly reduced compared to the case with a weaker headwind.

Temperature distributions in x-y planes from the aircraft centerplane to just outboard from the fuselage are shown in Fig. 15 The hot temperature region beneath the fuselage is more concentrated with the stronger headwind, and the stagnation region is much closer to the engine inlet

$U_\infty/V_j = 0.09$ and 0.03 at $H/D_j = 2$. A similar examination of the effect of the strength of the headwind is provided by comparing cases with $H/D_j = 2$ for the two headwind speeds used previously Smoothed near-ground temperature contours for these cases are shown in Fig. 16 (a) and (b). Partial temperature fields are shown in Fig. 17 in parts (a)-(d) and (e)-(h) for $U_\infty/V_j = 0.09$ and 0.03 respectively The corresponding velocity vector diagrams are in Fig. 18. Sequences of vertical x-y planes from the aircraft centerline to outboard of the fuselage are given in parts (a)-(d) and (e)-(h) in Fig 19 for both the strong and weak headwind cases.

For $U_\infty/V_j = 0.09$ (parts (a)-(d) in Figs 17-19), hot gases do not flow much farther upwind than the engine inlet, and the hot flow to the side of the fuselage is quickly swept to the rear by the strong headwind. The average dimensionless temperature rise at the face of the engine inlet is 0.03, and the maximum dimensionless temperature difference across the inlet is 0.34. These are both less than the comparable values for the same headwind velocity with $H/D_j = 4$ as shown in Tables 2 and 3.

Decreasing U_∞/V_j to 0.03 caused an increase in hot gas ingestion compared to the case with the stronger headwind. The average dimensionless inlet temperature rise was 0.11, and the maximum dimensionless temperature difference was 0.38. Hot gas penetrates much farther upwind in the case with the weaker headwind (cf parts (a) and (b) of Fig. 16). A flow at slightly greater than 45° to the aircraft fuselage centerline is also suggested by the temperature contours in Figs. 16(b) and 17 (e)-(h) and confirmed by the velocity vector diagrams in Fig. 18 (e)-(h). These also show much stronger side flow from the fountain area midway between the forward and aft jets in the case with a weaker headwind. This flow extends to planes above the base of the fuselage as shown in Figs. 17(h) and 18(h).

Vertical temperature fields are shown in parts (a)-(d) and (e)-(h) of Fig. 19 for $U_\infty/V_j = 0.09$ and 0.03 respectively. The flow field underneath the fuselage between the lift jets and the inlet is hotter for the strong headwind than for the weak headwind. Again note that the forward hot flow is stagnated much closer to the engine inlet by the stronger headwind. In the low speed case, the warm gases ingested by the inlet are much more diffuse than in the case with the stronger headwind.

Ground Proximity

$H/D_j = 2$ and 4 at $U_\infty/V_j = 0.09$. The average dimensionless engine inlet temperature rise was calculated to be 0.03 and 0.08 for cases with $U_\infty/V_j = 0.09$ for $H/D_j = 2$ and 4 respectively The maximum dimensionless temperature difference for these cases was 0.34 and 0.44. Although the mean temperature of the gas ingested by the engine inlet is less when the ground is closer to the base of the aircraft fuselage, temperatures near the lift jet system are higher (cf. Figs. 15 and 19 (a)-(d)). Not surprisingly, the side flow from the fountain area is noticeably stronger and hotter with the aircraft closer to the ground (cf. Figs. 13 and 17 (a)-(d)).

A comparison of the vector plots in Figs. 14 and 18 (a)-(d) also shows the side flow to be stronger with the aircraft closer to the ground. However, the flow to the rear of the aft lift jets appears to be hotter when the aircraft is farther from the ground (cf. Figs. 15 and 19 (a)-(d)). The general shape of the ground temperature field is apparently more dependent on the headwind velocity than the ground proximity since the two cases considered here are quite similar, as can be seen by comparing the two smoothed ground plane temperature distributions in Figs. 12 and 16(a).

The vertical x-y temperature distributions in Figs. 15 and 19 (a)-(d) show a different temperature profile for the region underneath the forward fuselage for the two distances between the base of the fuselage and the ground. For $H/D_j = 4$ the warm gases are seen farthest forward near the ground, whereas for $H/D_j = 2$ the hot gases are farthest forward just beneath the base of the fuselage.

Velocity vector diagrams in vertical planes through the engine inlet duct and lift jets are shown in Fig. 20. Parts (b) and (c) are for $H/D_j = 4$ and $H/D_j = 2$ with $U_\infty/V_j = 0.09$. Part (c) shows headwind flow near the ground much closer to the front lift jets than does part (b). This would account for lower temperatures in this portion of the flow field for the $H/D_j = 2$ case.

$H/D_j = 2$ and 4 at $U_\infty/V_j = 0.03$. The average dimensionless engine inlet temperature rise was calculated to be 0.11 and 0.13 for cases with a weaker headwind of $U_\infty/V_j = 0.03$ for $H/D_j = 2$ and 4 respectively. These values of the mean temperature rise are slightly higher (the flow in the inlet is warmer) than at the same heights above the ground for the stronger headwind. Calculated values of the maximum dimensionless temperature difference for the cases with the weaker headwind were 0.38 and 0.30. Although these values are comparable to those for the stronger headwind, the larger value (0.38) occurs at $H/D_j = 2$ for $U_\infty/V_j = 0.03$, whereas the larger value (0.44) occurred at $H/D_j = 4$ for $U_\infty/V_j = 0.09$.

Ground plane temperature distributions for both cases with $U_\infty/V_j = 0.03$ are shown in Figs. 6 and 16(b). Both show the oblique forward flow cited previously, with the $H/D_j = 4$ case showing slightly more oblique penetration into the headwind (cf. Figs. 9(a) and 10(a) to Figs. 17(e) and 18(e)). However the $H/D_j = 2$ case shows much more forward penetration along the aircraft centerline. Upwind flow was observed up to $35(D_j)$ ahead of the engine inlet for the $H/D_j = 2$ case versus about $28(D_j)$ for the $H/D_j = 4$ case. As seen previously, more side flow from the fountain is seen for the $H/D_j = 2$ case, whereas hotter flow to the rear is shown for the $H/D_j = 4$ case. Comparison of the vertical temperature distributions in Figs. 11 and 19(e)-(h) shows the flow is generally cooler underneath the fuselage for the $H/D_j = 4$ case except downwind of the rear lift jet.

Velocity vector diagrams in vertical planes through the engine inlet duct and lift jets are shown for $H/D_j = 4$ and $H/D_j = 2$ with $U_\infty/V_j = 0.03$ in parts (a) and (d) of Fig. 20. All parts of this figure clearly show the recirculation zones between the forward jets and the fountain, and between the fountain and the aft jets. For both cases with $H/D_j = 4$ (parts (a) and (b)), the area between the first lift jet and fountain is noticeably cooler than between the fountain and rear lift jets (Figs. 11 and 15). The horizontal velocity vector diagrams for cases with $U_\infty/V_j = 0.03$, Figs. 10(b) and 18(f), show flow coming into this area for the $H/D_j = 4$ case, while flow is outward from the hot fountain area for the $H/D_j = 2$ case.

Inlet Temperatures

Figure 21 shows the temperature distributions in the first axial plane of the inlet duct for all four cases calculated. A different temperature scale has been used on this figure to better show the range and distribution of temperatures in the engine inlet. All of the distributions show highest temperatures along the lower inside corner. The weaker headwind cases (a) and (c) show a larger volume of hot gas underneath the fuselage at this point. The stronger headwind cases ((b) and (d)) show higher temperatures right at the base of the fuselage for this axial location, which is a prime location for hot gas ingestion.

Summary

Hot gas ingestion was predicted for all reported cases. The primary flowpath for ingestion was underneath the front part of the fuselage. With strong headwinds, the hot gas ingestion was a combination of flow directly along the bottom of the fuselage and hot flow from the lift jet area stagnating slightly upwind of the engine inlet underneath the front part of the fuselage. Weaker headwinds allowed the forward flow from the fountain area to penetrate much farther upwind allowing the hot flow to mix around the side of the forward part of the fuselage where some of it was ingested. Direct ingestion from the fountain-lift jet area was seen for all cases. The mean inlet temperature rise increased with decreasing headwind strength and decreasing distance from the ground. No such clear-cut pattern was shown for the maximum temperature distortion in the four calculations with the maximum temperature difference at $U_\infty/V_j = 0.09$ observed for $H/D_j = 4$ and for $H/D_j = 2$ at $U_\infty/V_j = 0.03$.

The TEACH-type code used was successful in predicting temperature and velocity distributions in a VSTOL flow field. Accuracy could be improved with more accurate numerical differencing schemes and more gridpoints. Both of these require the use of larger and faster computers. Some modification of the code is needed for transonic and supersonic flows. Also, having body-fitted coordinates would allow modeling of a more realistic aircraft than the box-like structure used for the present calculations. These modifications will be undertaken in the future so that CFD can be used in the ASTOVL design process as a powerful design tool in concept analysis.

References

1 Kuhn, R.E., "Design Concepts for Minimizing Hot-Gas Ingestion in V/STOL Aircraft," Journal of Aircraft, Vol. 19, No. 10, Oct 1982, pp. 845–850.

2. Kuhn, R.E., and Eshelman, J., "Ground Effects on V/STOL and STOL Aircraft—A Survey," AIAA Paper 85–4033, Oct. 1985. (NASA TM–86825).

3. Claus, R.W., "Numerical Calculation of Subsonic Jets in Crossflow with Reduced Numerical Diffusion," AIAA Paper 85–1441, July 1985. (NASA TM–87003).

4. Mongia, H.C, Reynolds, R.S., and Srinivasan, R., "Multi-Dimensional Gas Turbine Combustion Modeling Applications and Limitations," AIAA Journal, Vol. 24, No. 6, June 1986, pp. 890–904.

5 Turan, A., and VanDoormal, J.P, "Improved Numerical Methods for Turbulent Viscous Recirculating Flows," NASA CR–180852, 1987

6. Holdeman, J.D., Mongia, H.C, and Mularz, E.J, "Assessment, Development, and Application of Combustor Aerothermal Models," NASA TM–100290, 1988.

7 "V/STOL Aircraft Aerodynamics," Vol. I, C Henderson and M.F Platzer, eds., 1979 (Avail NTIS, AD–079115). "V/STOL Aircraft Aerodynamics," Vol. II, C Henderson and M.F Platzer, eds., 1979 (Avail NTIS, AD–078909).

8. "Special Course on V/STOL Aerodynamics," AGARD–R–710, AGARD, Neuilly-Sur-Seine, France, 1984. (Avail. NTIS, AD–A144214).

9. "Proceedings of the 1985 NASA Ames Research Center's Ground Effects Workshop," NASA CP–2462, K. Mitchell, ed., NASA, Washington, D.C, 1985.

10. "Proceedings of the 1987 International Powered Lift Conference," Santa Barbara, CA, SAE P–88–203, 1987, to be published.

11 Syed, S.A., and James, R.H, "User Manual for 3D-Teach With Rotation," NASA CR–180886, 1988.

12 Patankar, S.V., and Shih, T.M, Numerical Heat Transfer and Fluid Flow, Hemisphere Publishing Corp., Washington, D.C, 1980.

13. Syed, S.A, Chiapetta, L.M., and Gosman, A.D., "Error Reduction Program," PWA–5928–25, Pratt & Whitney Aircraft, East Hartford, CT, 1985, NASA CR–174776.

14. Patankar, S.V., Karki, K.C, and Mongia, H.C., "Development and Evaluation of Improved Numerical Schemes for Recirculating Flows," AIAA Paper 87–0061, Jan. 1987

15. Runchal, A.K., Anand, M.S., and Mongia, H.C., "An Unconditionally-Stable Central Differencing Scheme for High Reynolds Number Flows," AIAA Paper 87–0060, Jan. 1987

16. Vanka, S.P, "Block-Implicit Computation of Viscous Internal Flows—Recent Results," AIAA Paper 87–0058, Jan. 1987

17 Przekwas, A.J, Singhal, A.K., and Tam, L.T, "Rocket Injector Anomalies Study, Vol I: Description of Mathematical Model and Solution Procedures," CHAM–H3605/15–VOL–1, CHAM of North America, Huntsville, AL, 1984, NASA CR–174702.

18. Van Doormal, J.P, "Numerical Methods for the Solution of Imcompressible and Compressible Fluid Flows," Ph.D. Thesis, University of Waterloo, Canada, 1985.

19. Karki, K.C, "A Calculation Procedure for Viscous Flows at all Speeds in Complex Geometries," Ph.D. Thesis, University of Minnesota, 1986.

20. "Graph3D· Interactive 3–D Computer Graphics Users Guide," NASA Lewis Research Center, Cleveland, OH, 1985.

21 Johns, A., Flood, J.D., and Strock, T.W., "A Vectored Thrust STOVL Concept With Flow Visualization in the NASA Lewis 9′ × 15′ Low Speed Wind Tunnel," AIAA Paper 88–3025, July 1988

22. Gray, L., and Kisielowski, E., "Practical Engineering Methods for Predicting Hot Gas Reingestion Characteristics of V/STOL Aircraft Jet Lift Engines," DCR–323, Dynasciences Corp., Blue Bell, PA, 1971, NASA CR–111845

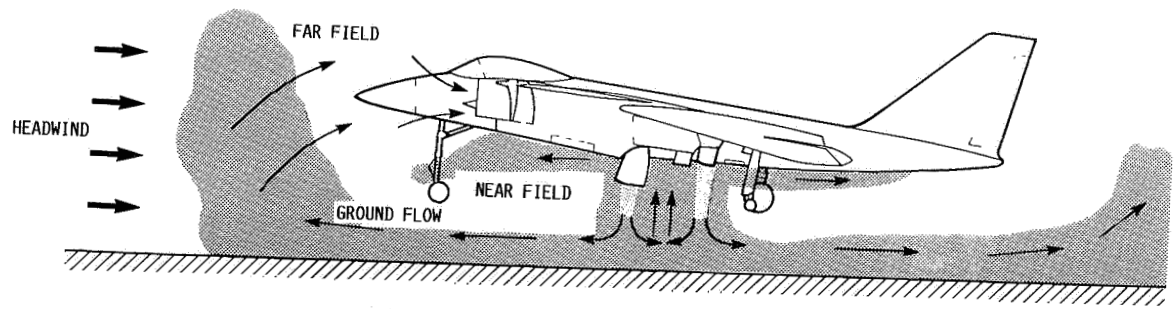

Fig. 1 Hot gas ingestion mechanisms.

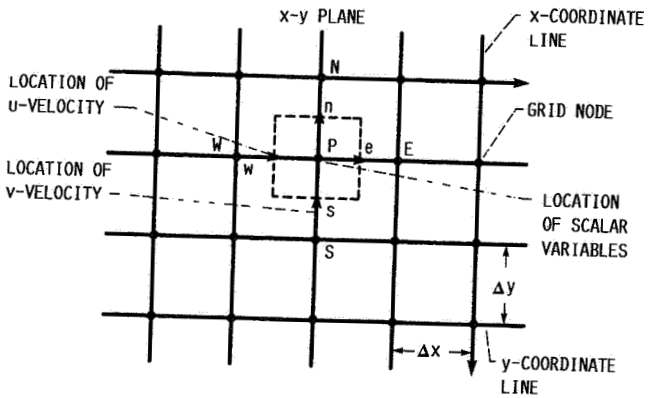

Fig. 2 Typical computational cell in x-y plane.

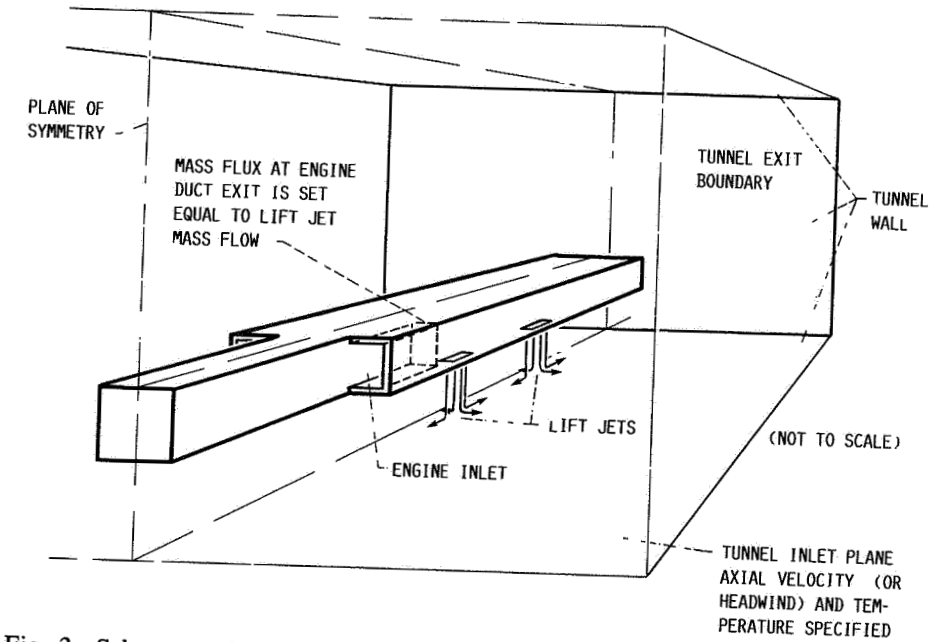

Fig. 3 Schematic of calculation domain. Mass flow at tunnel exit is set equal to tunnel inlet mass flow

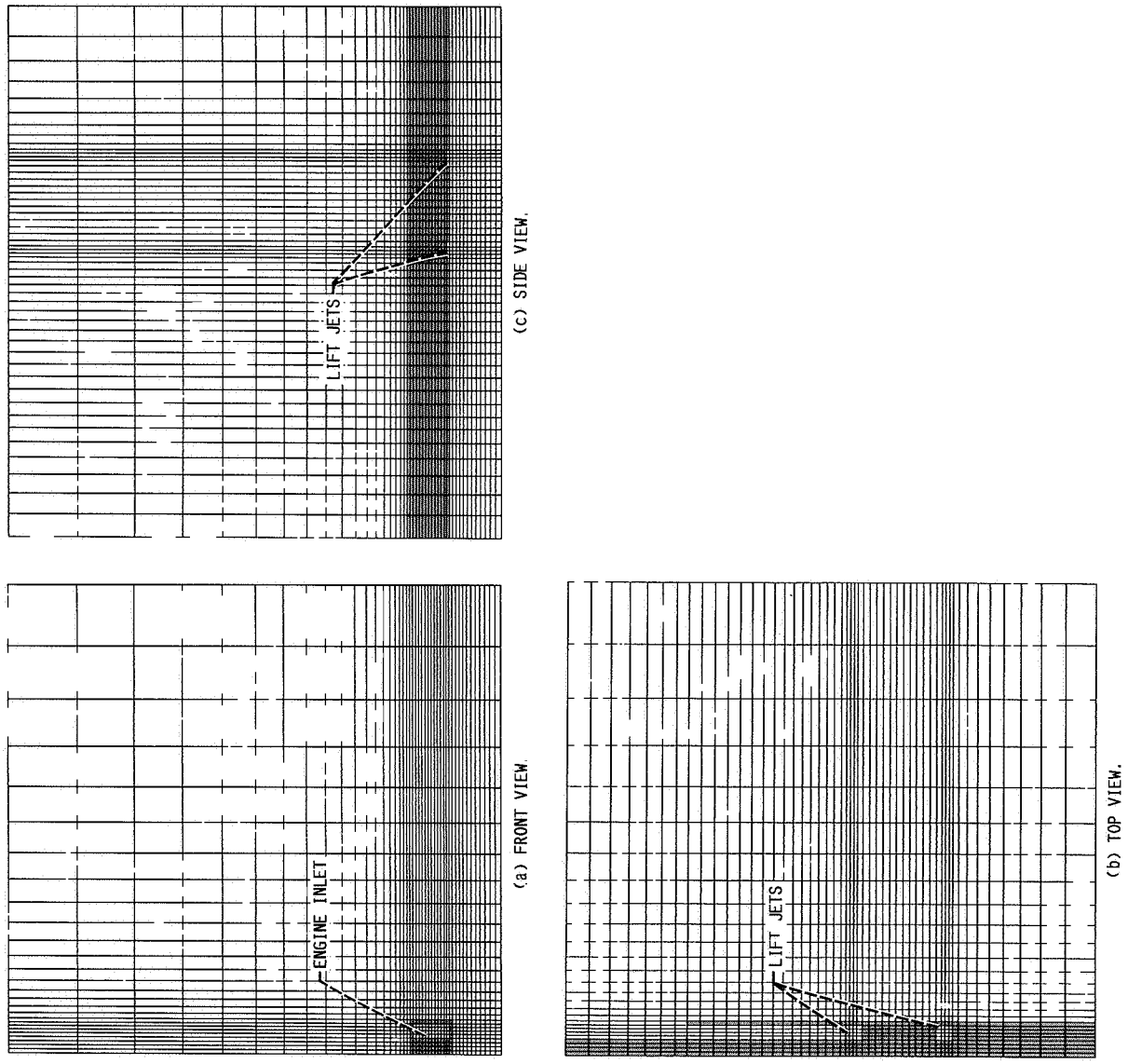

Fig. 4 Numerical grid.

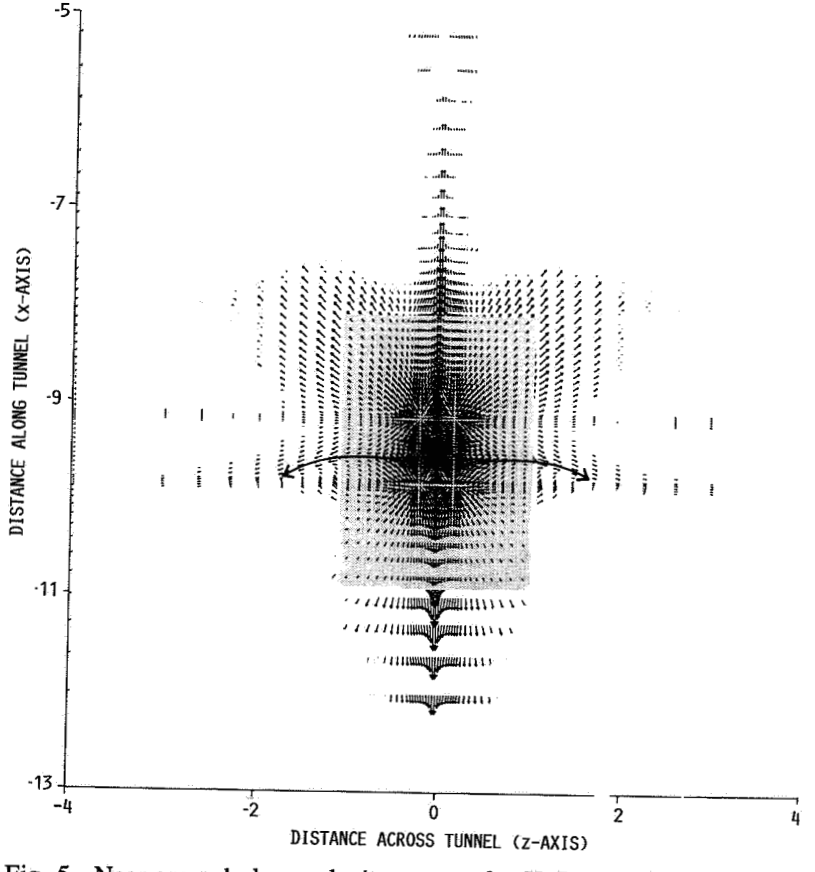

Fig. 5 Near ground-plane velocity vectors for $H/D_j = 4$, $U_\infty/V_j = 0.03$. (Velocity vectors in shaded zone are plotted a factor of 4 smaller than outside area).

Fig 6 Smoothed ground-plane temperature distribution for $H/D_j = 4$, $U_\infty/V_j = 0.03$.

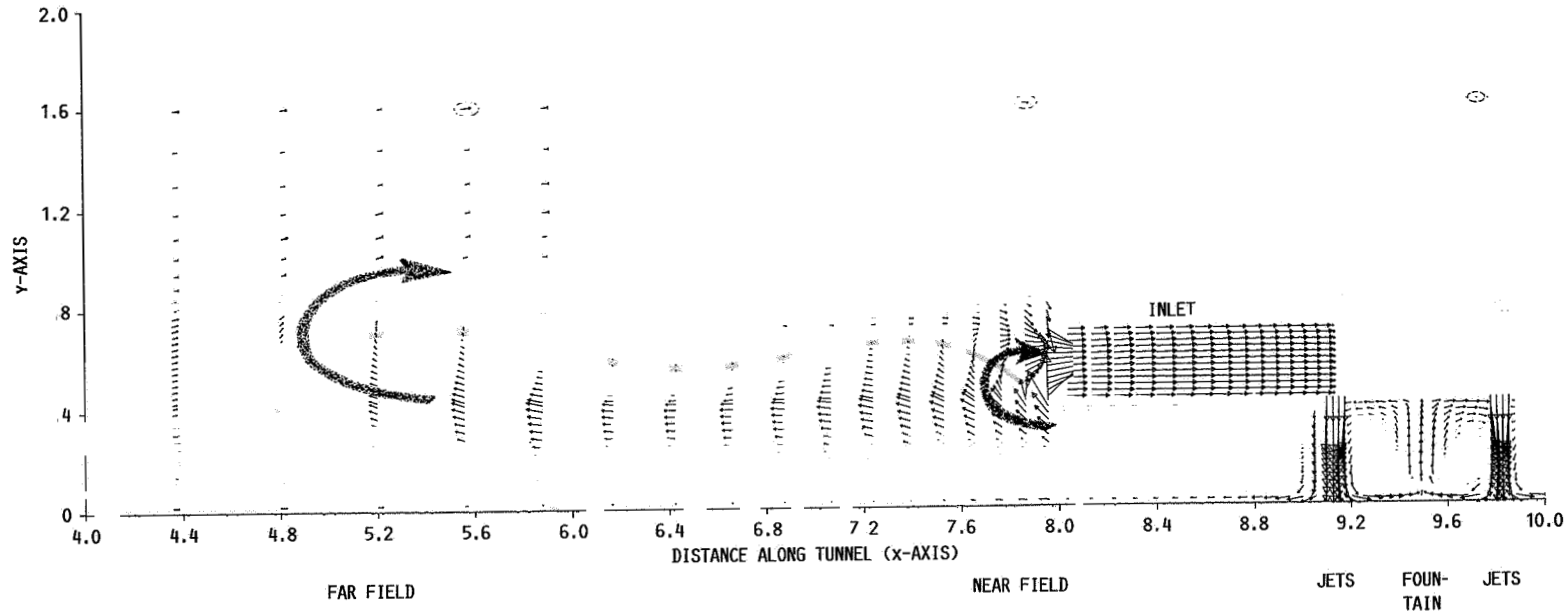

Fig. 7 Velocity vectors in vertical plane through engine inlet and lift jets for $H/D_j = 4$, $U_\infty/V_j = 0.03$ (plotted at different velocity scales). Circled arrow represents approximately 30 ft/sec.

ORIGINAL PAGE
COLOR PHOTOGRAPH

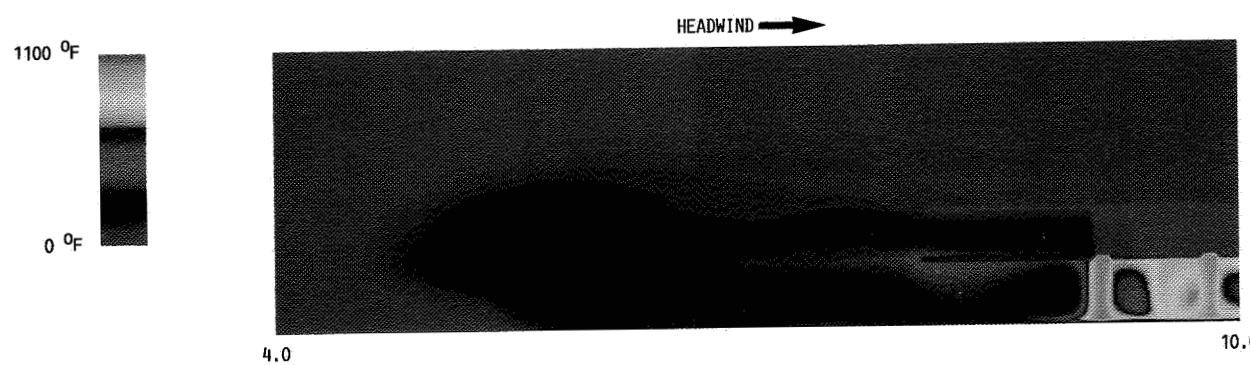

Fig. 8 Smoothed temperature distribution in vertical plane through engine inlet and lift jets for $H/D_j = 4$, $U_\infty/V_j = 0.03$.

ORIGINAL PAGE
COLOR PHOTOGRAPH

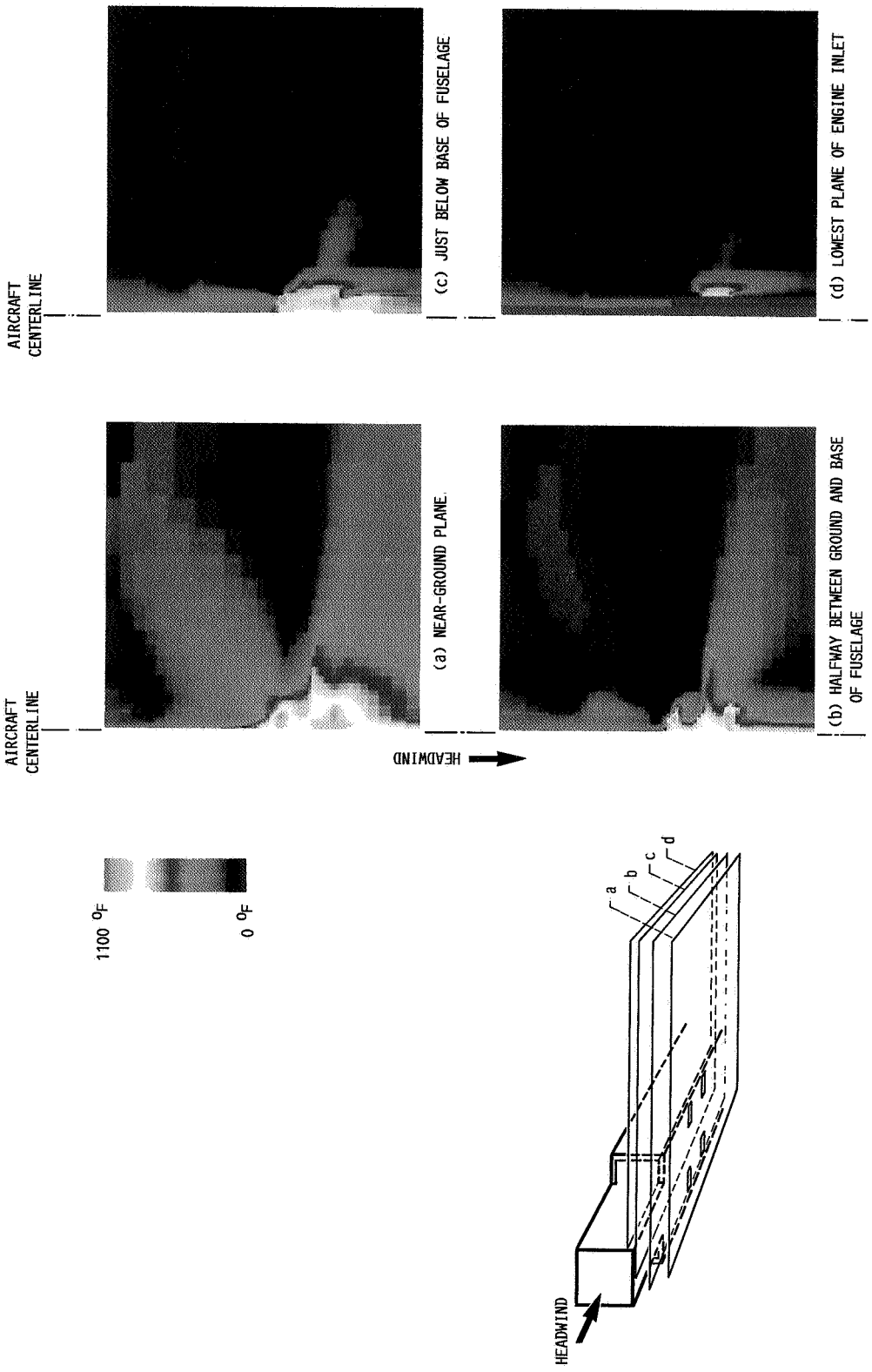

Fig. 9 Temperature distribution in horizontal planes for $H/D_j = 4$, $U_\infty/V_j = 0.03$.

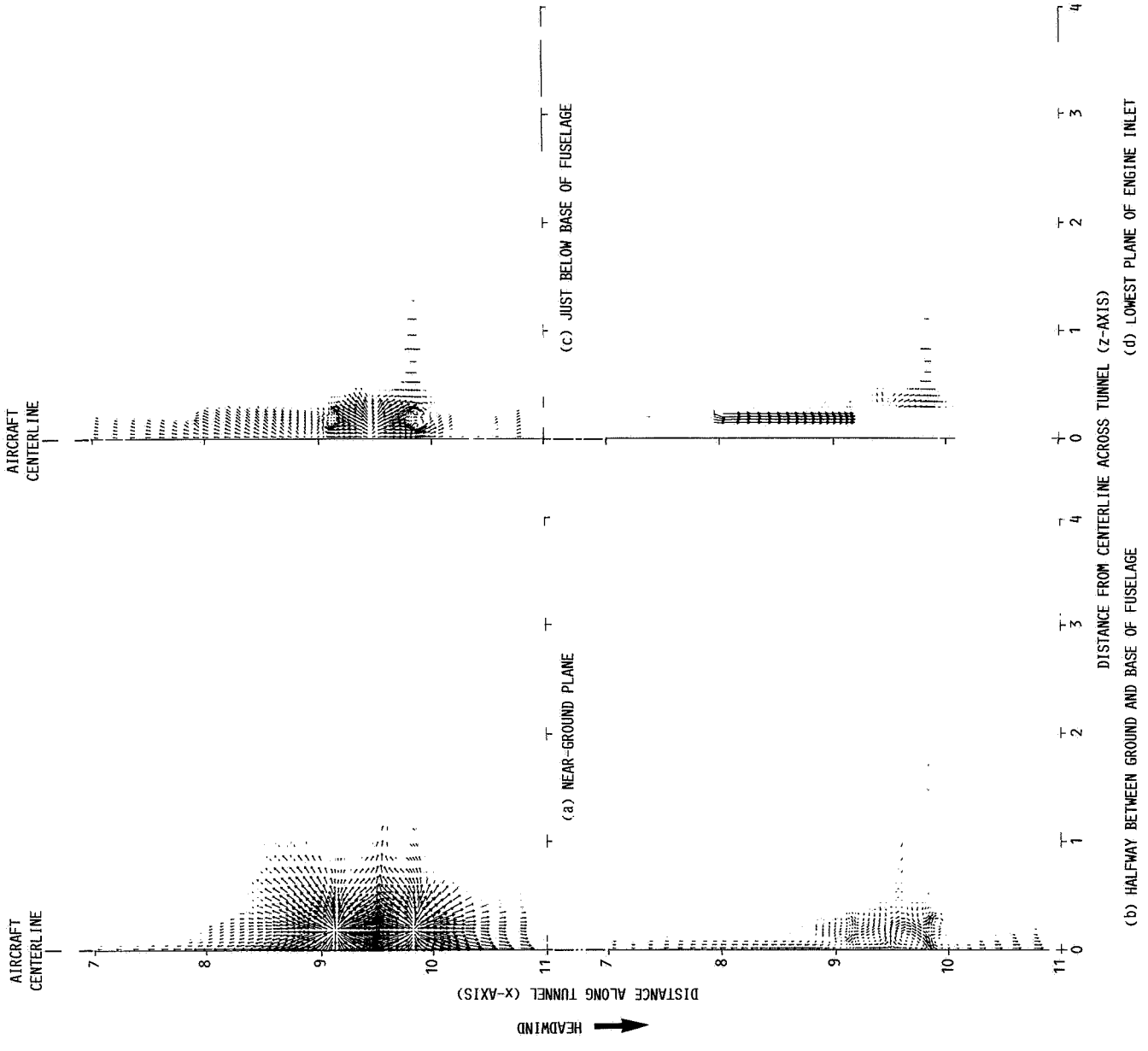

Fig. 10 Velocity vectors in horizontal planes for $H/D_j = 4$, $U_\infty/V_j = 0.03$

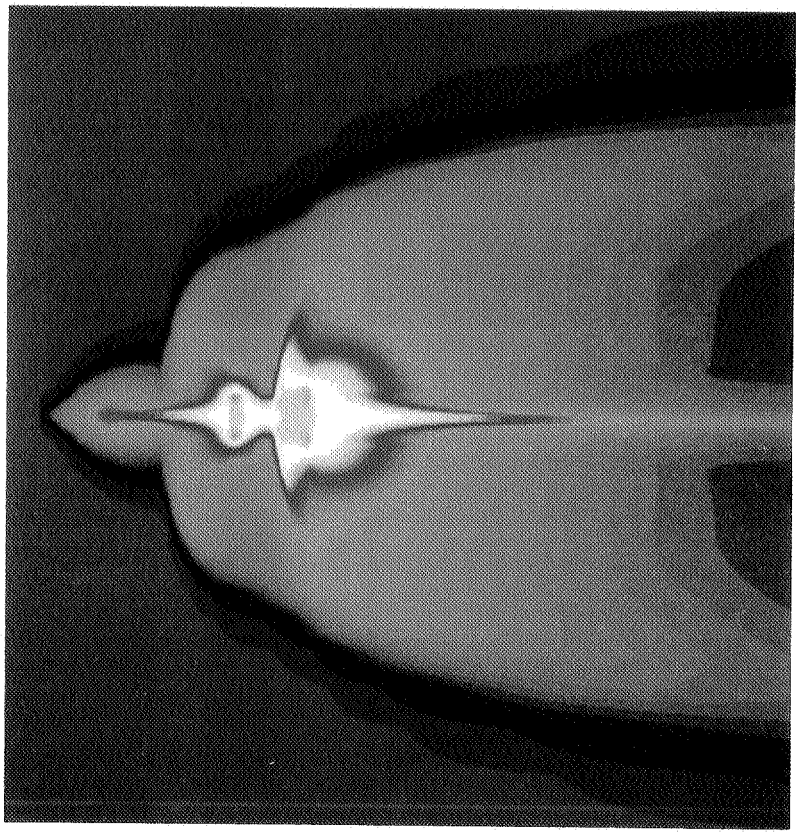

Fig. 12 Smoothed ground-plane temperature distribution for $H/D_j = 4$, $U_\infty/V_j = 0.09$

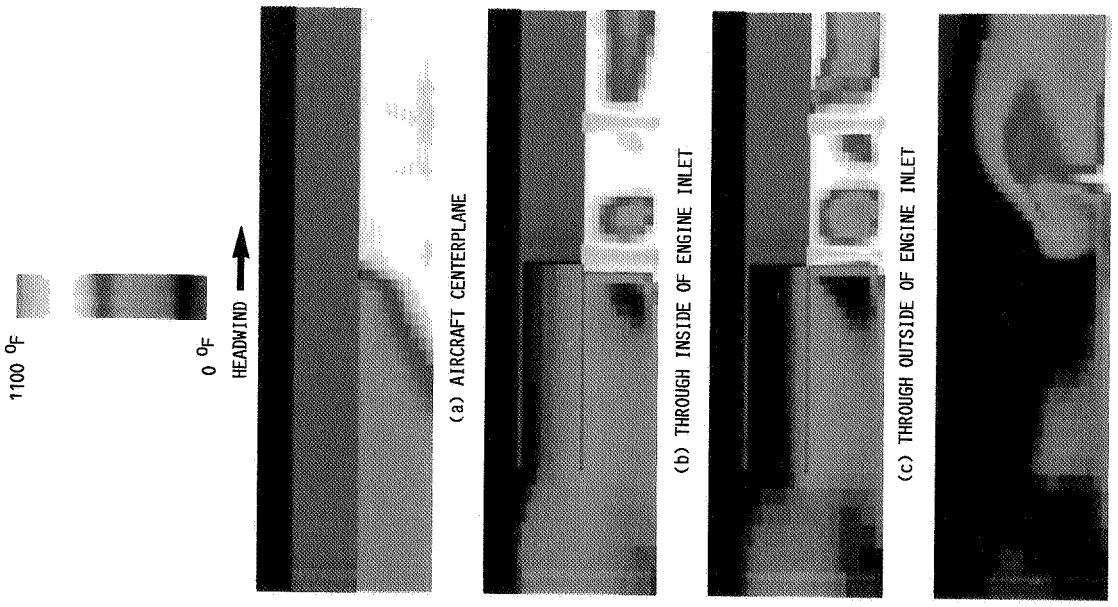

Fig. 11 Temperature distribution in vertical planes for $H/D_j = 4$, $U_\infty/V_j = 0.03$.

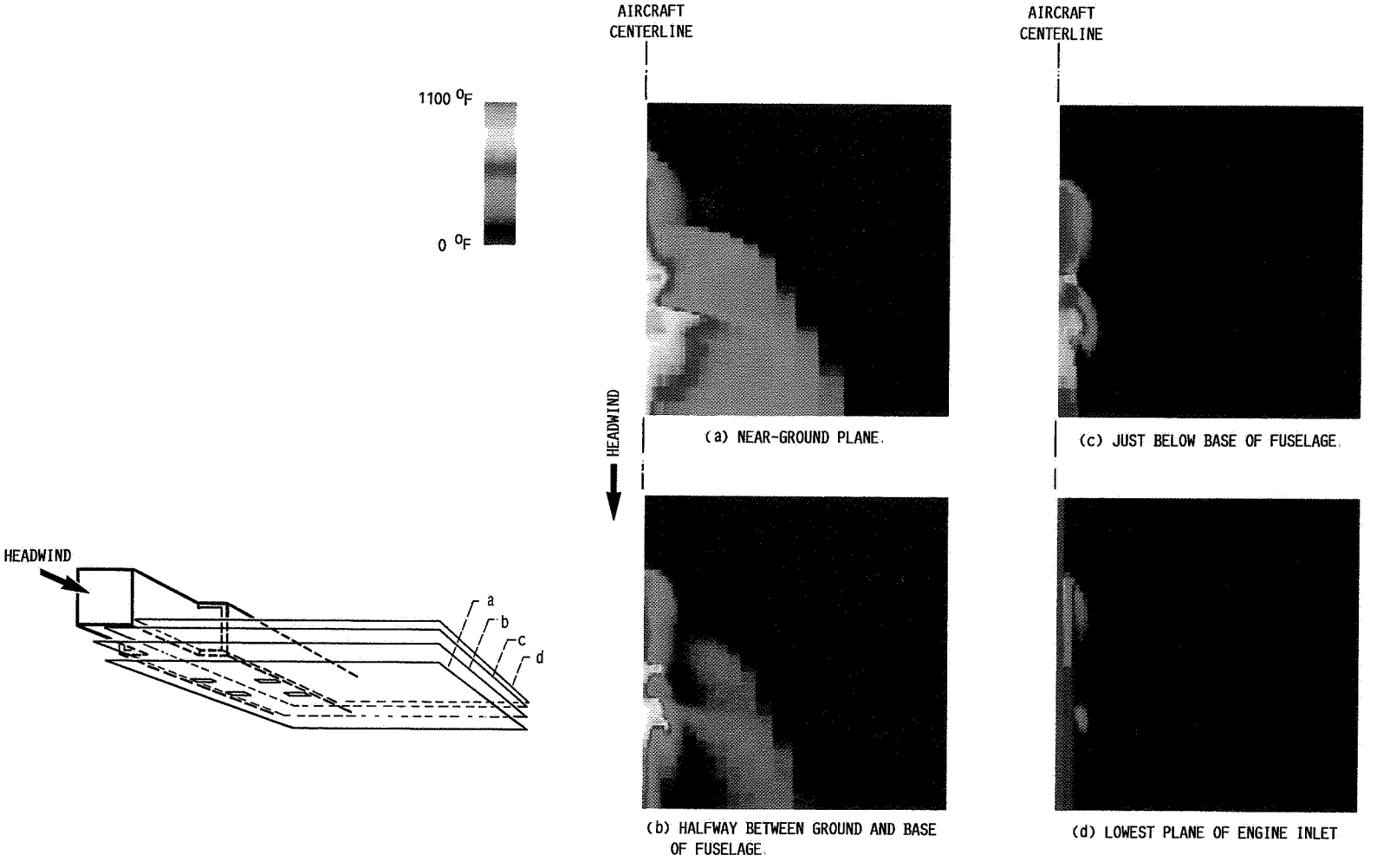

Fig. 13 Temperature distribution in horizontal planes for $H/D_j = 4$, $U_\infty/V_j = 0.09$.

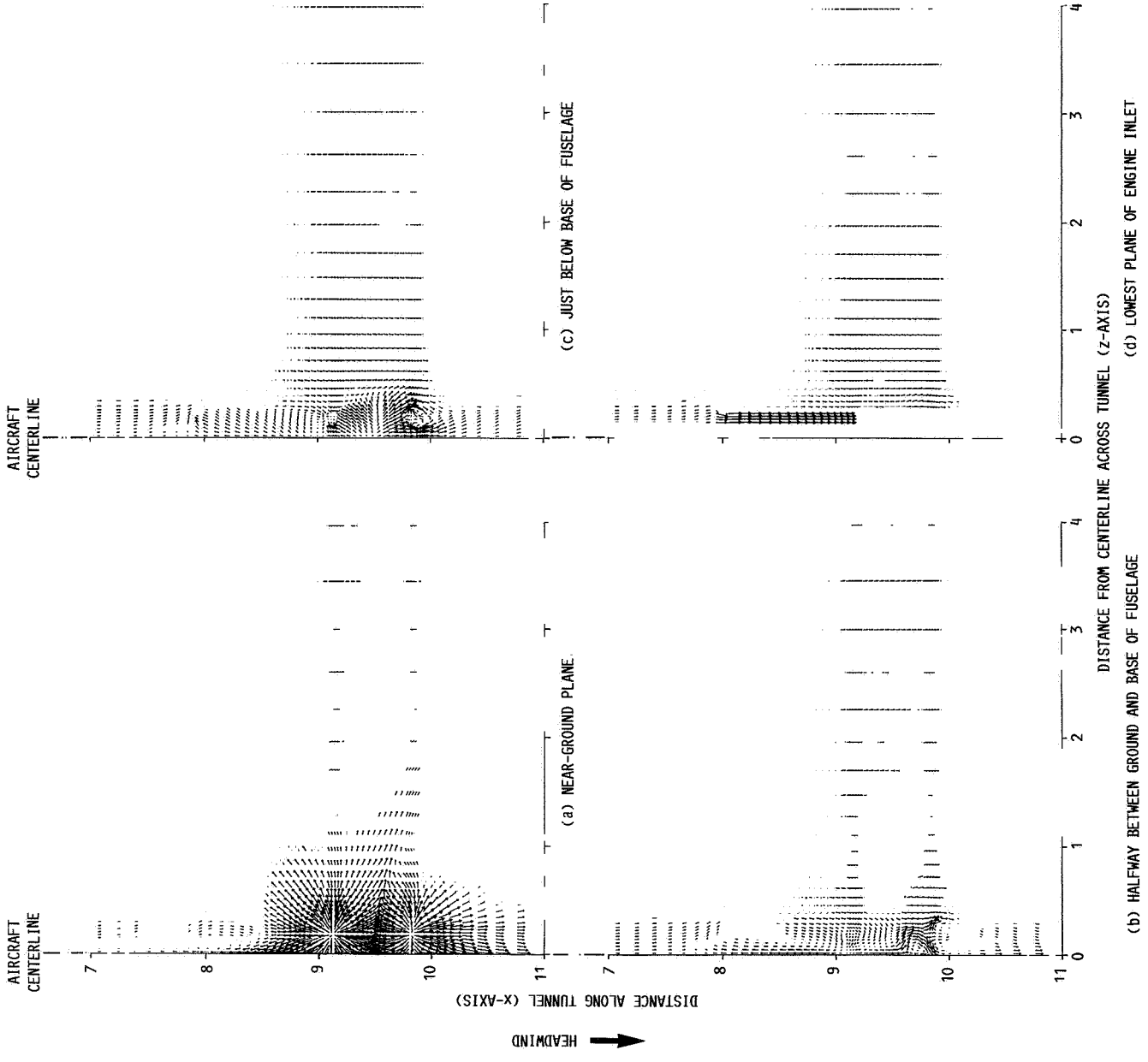

Fig. 14 Velocity vectors in horizontal planes for $H/D_j = 4$, $U_\infty/V_j = 0.09$

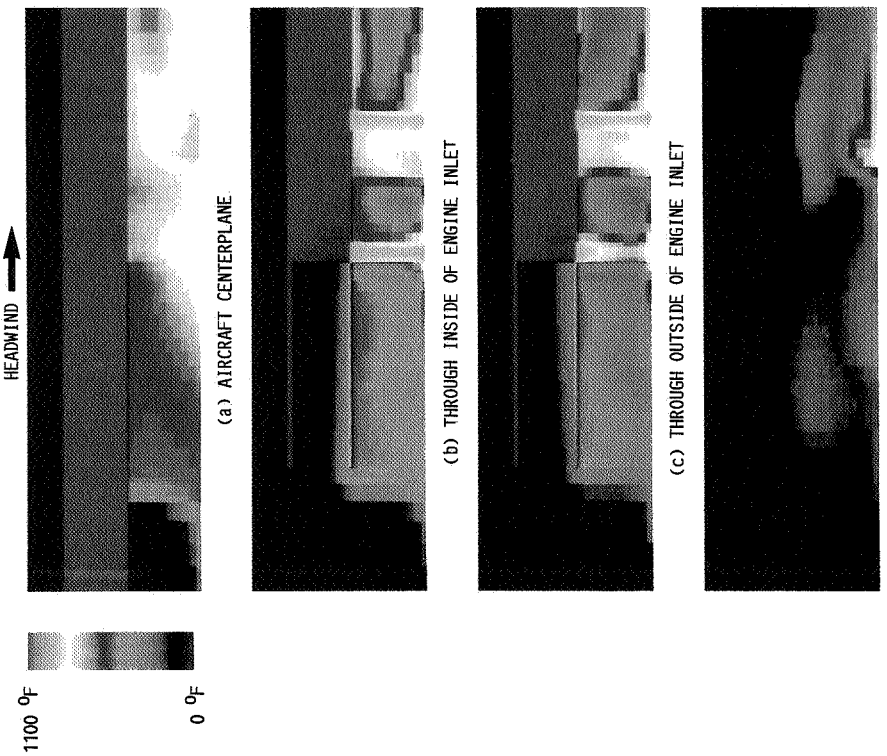

Fig. 15 Temperature distribution in vertical planes for $H/D_j = 4$, $U_\infty/V_j = 0.09$

ORIGINAL PAGE
COLOR PHOTOGRAPH

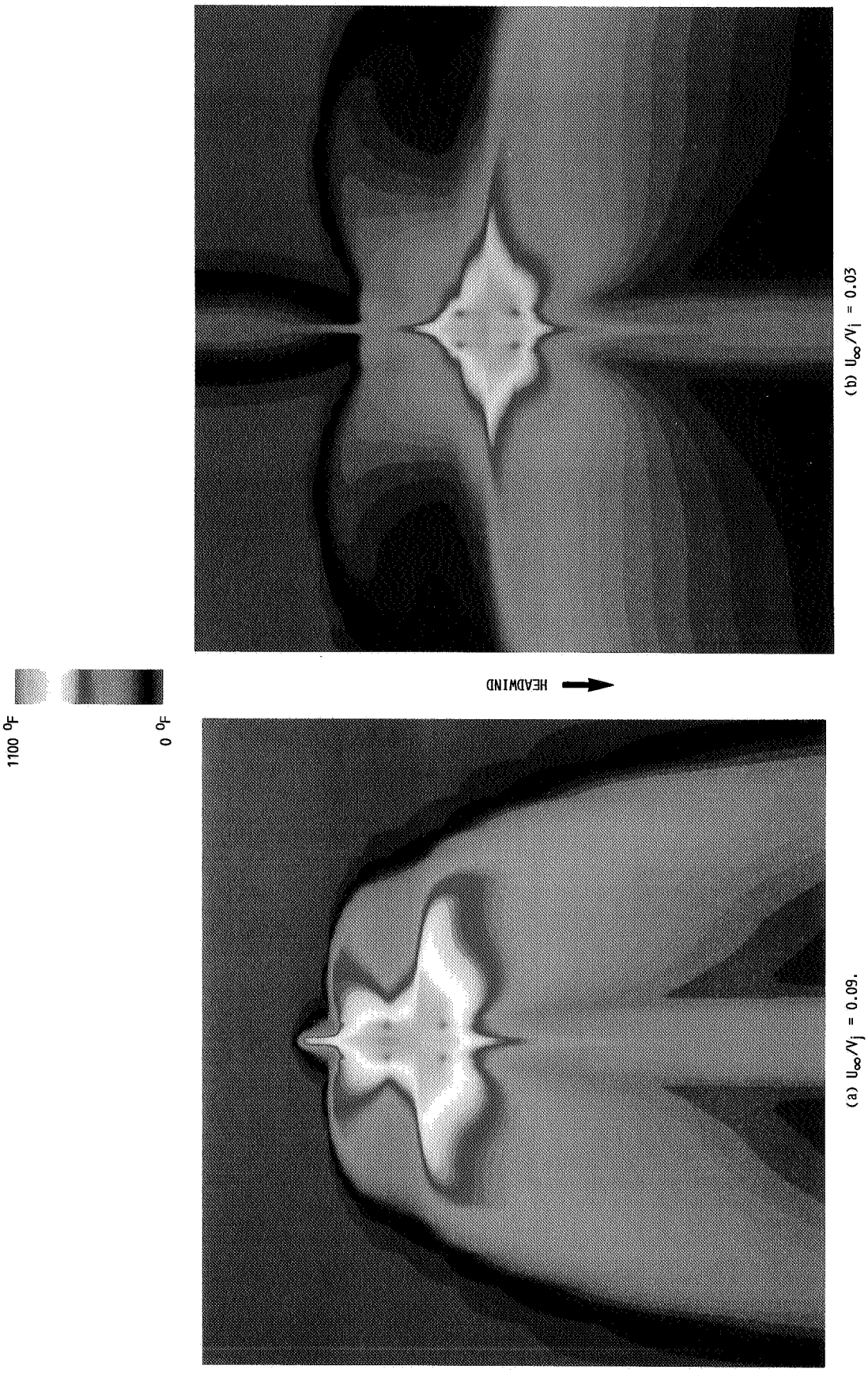

Fig. 16 Smoothed ground-plane temperature distributions for $H/D_j = 2$

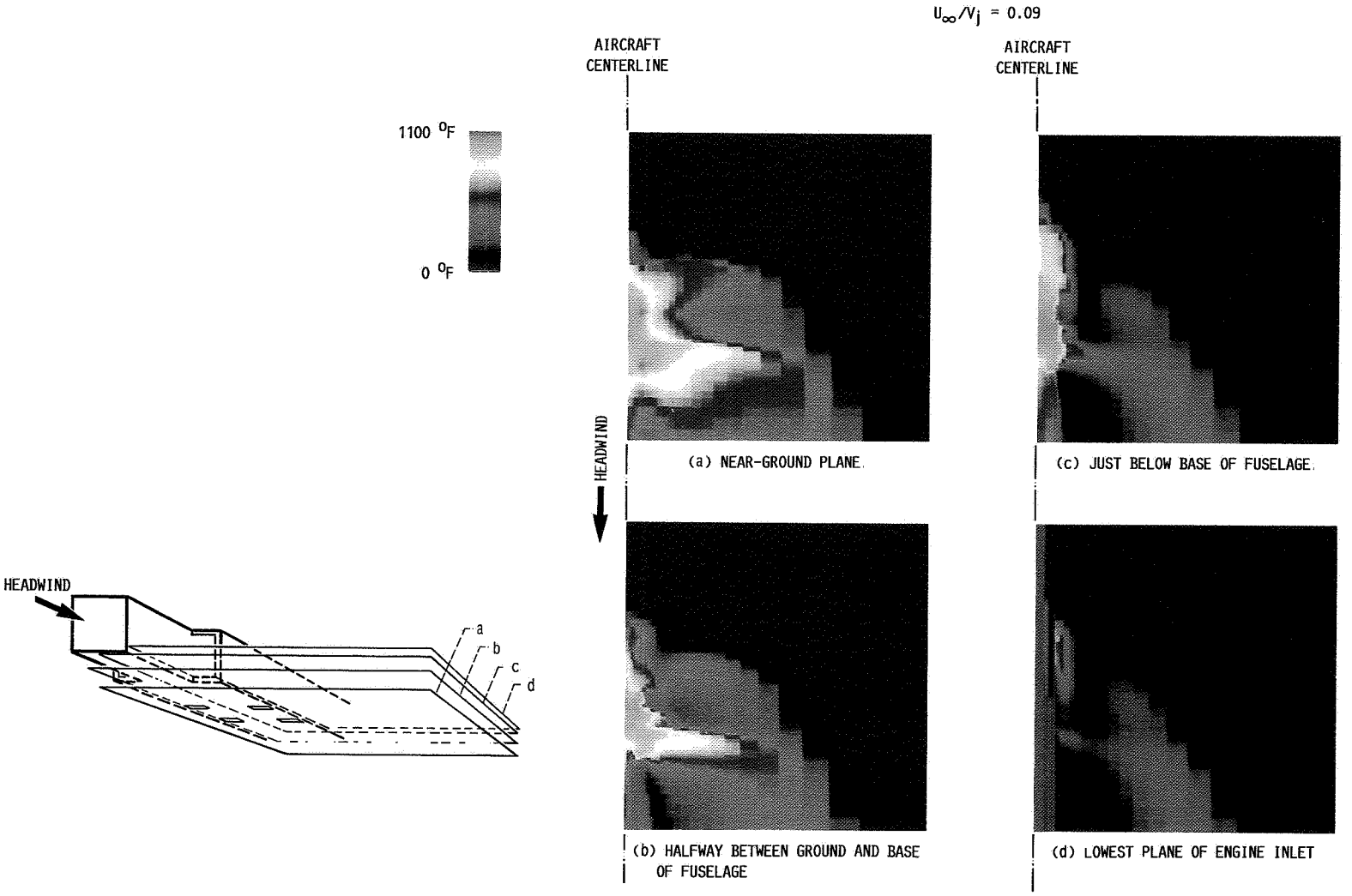

Fig. 17 Temperature distributions in horizontal planes for $H/D_j = 2$.

ORIGINAL PAGE
COLOR PHOTOGRAPH

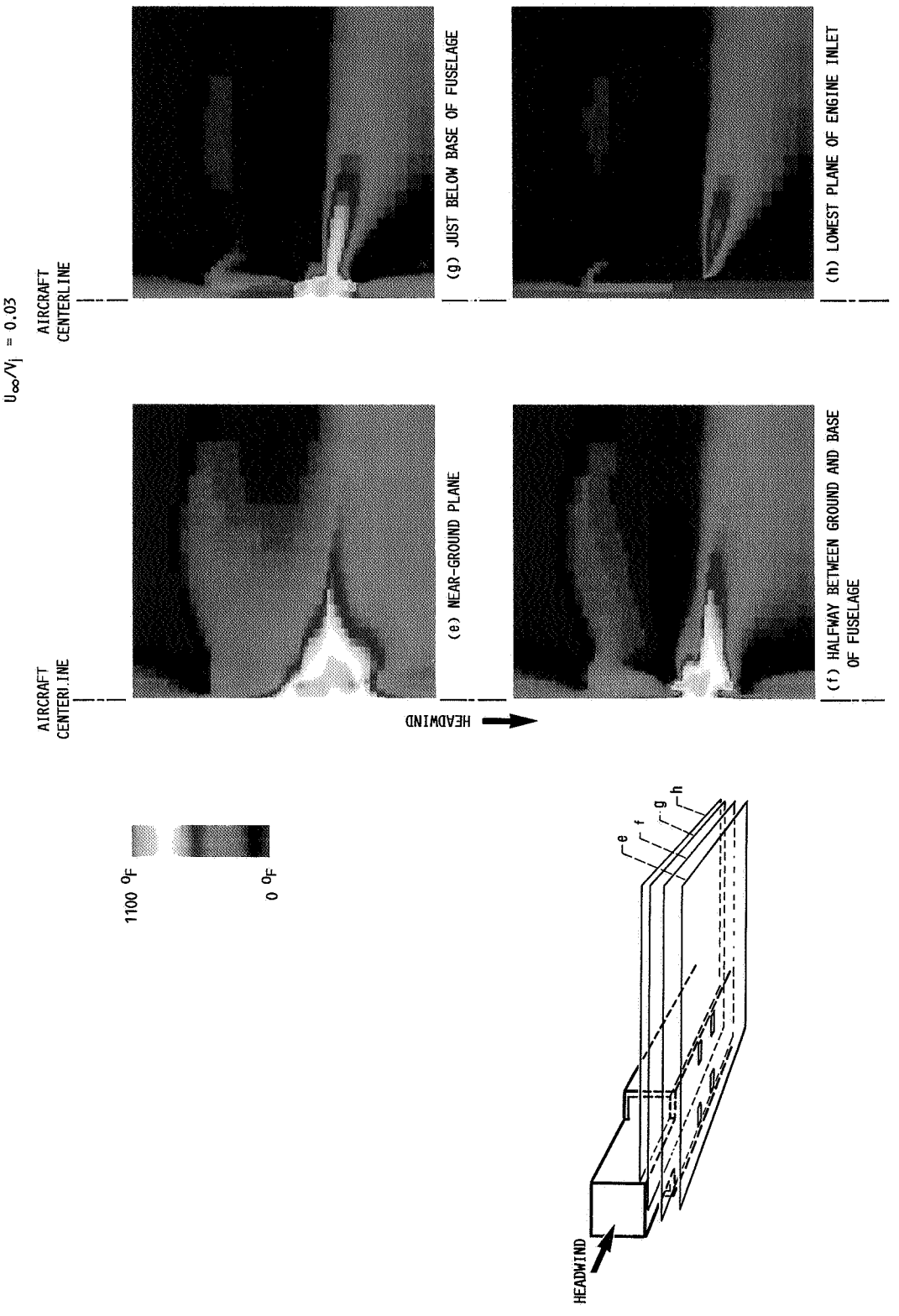

Fig 17 Concluded

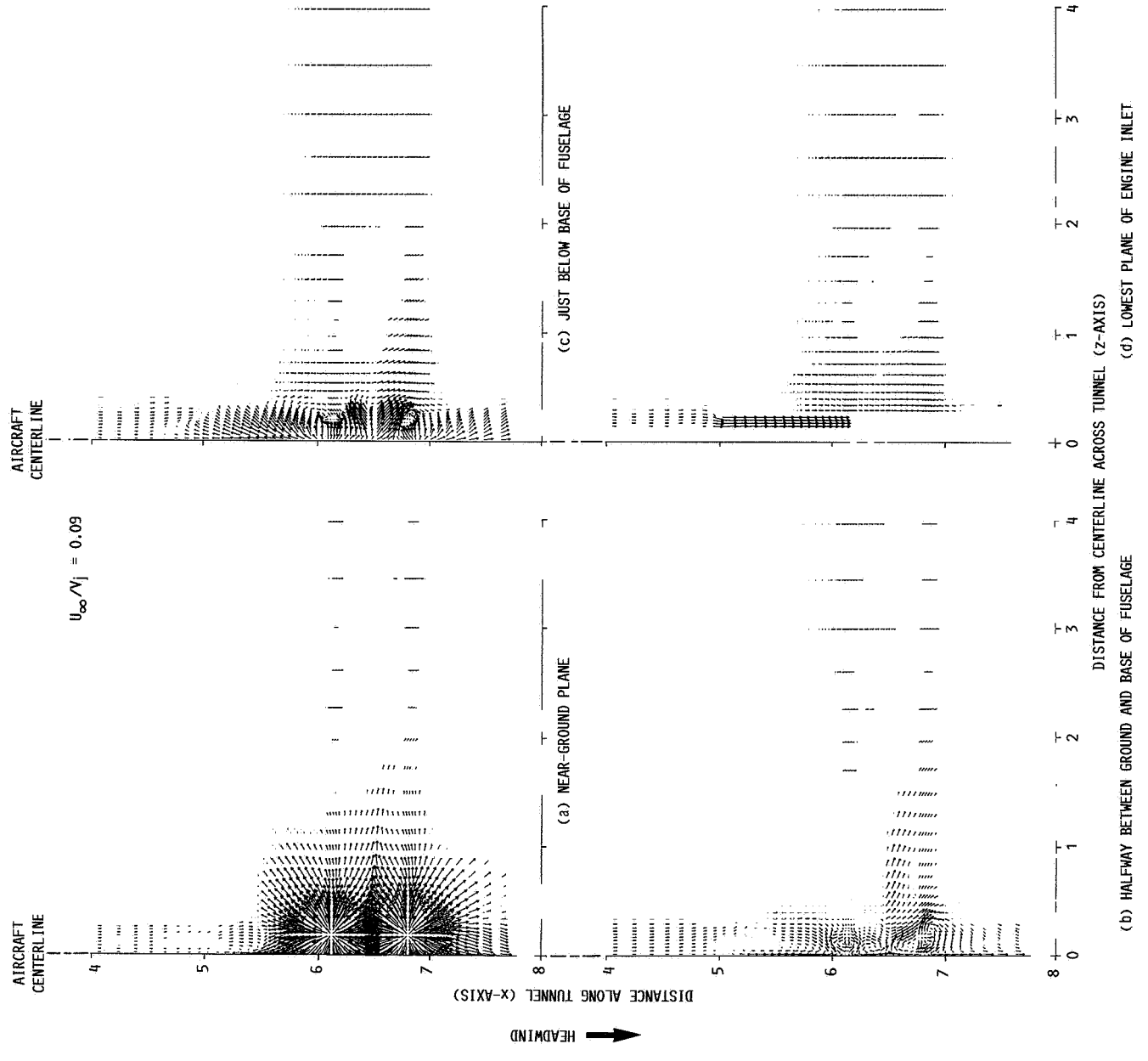

Fig. 18 Velocity vector distributions in horizontal planes for $H/D_j = 2$.

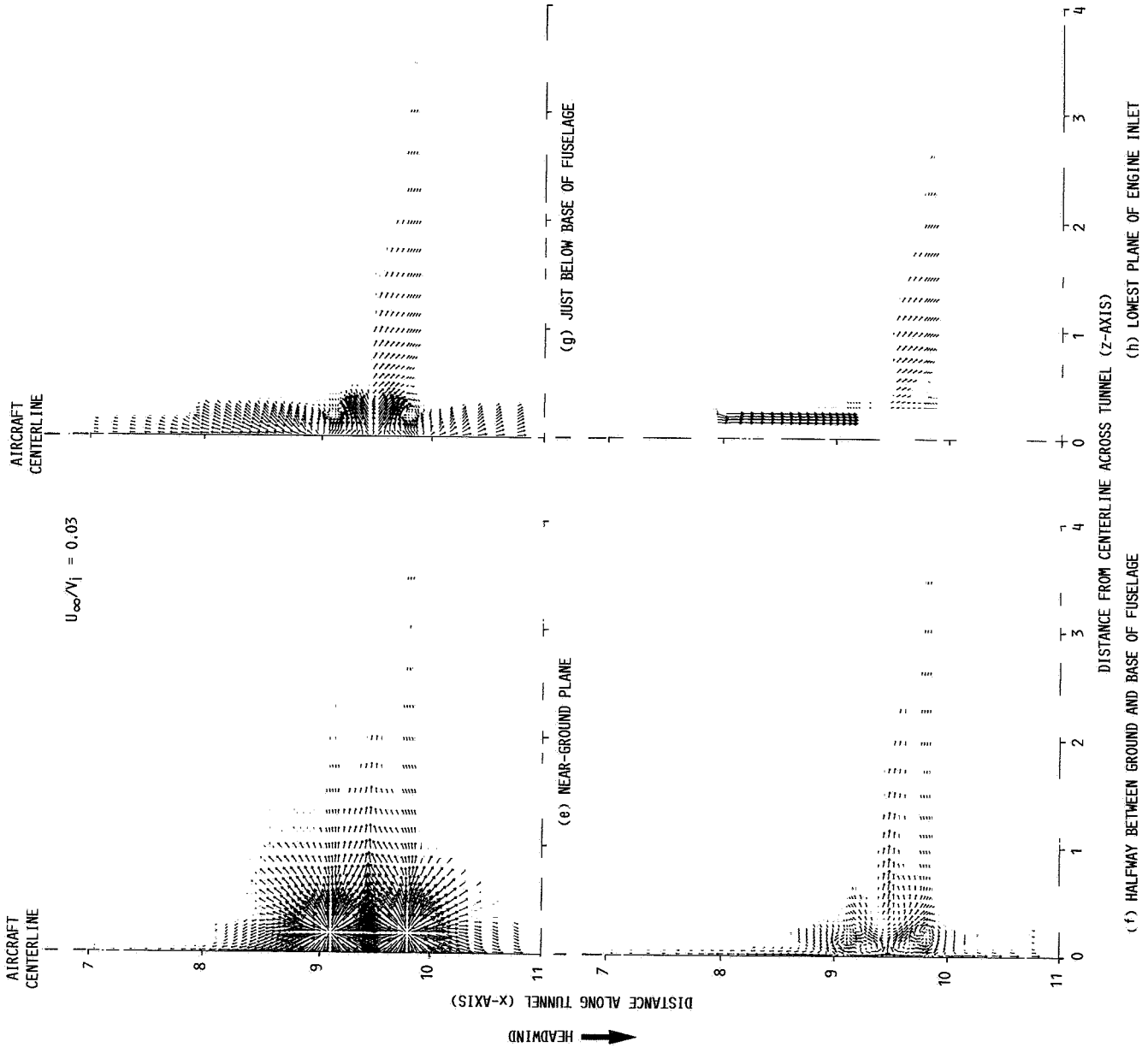

Fig. 18 Concluded.

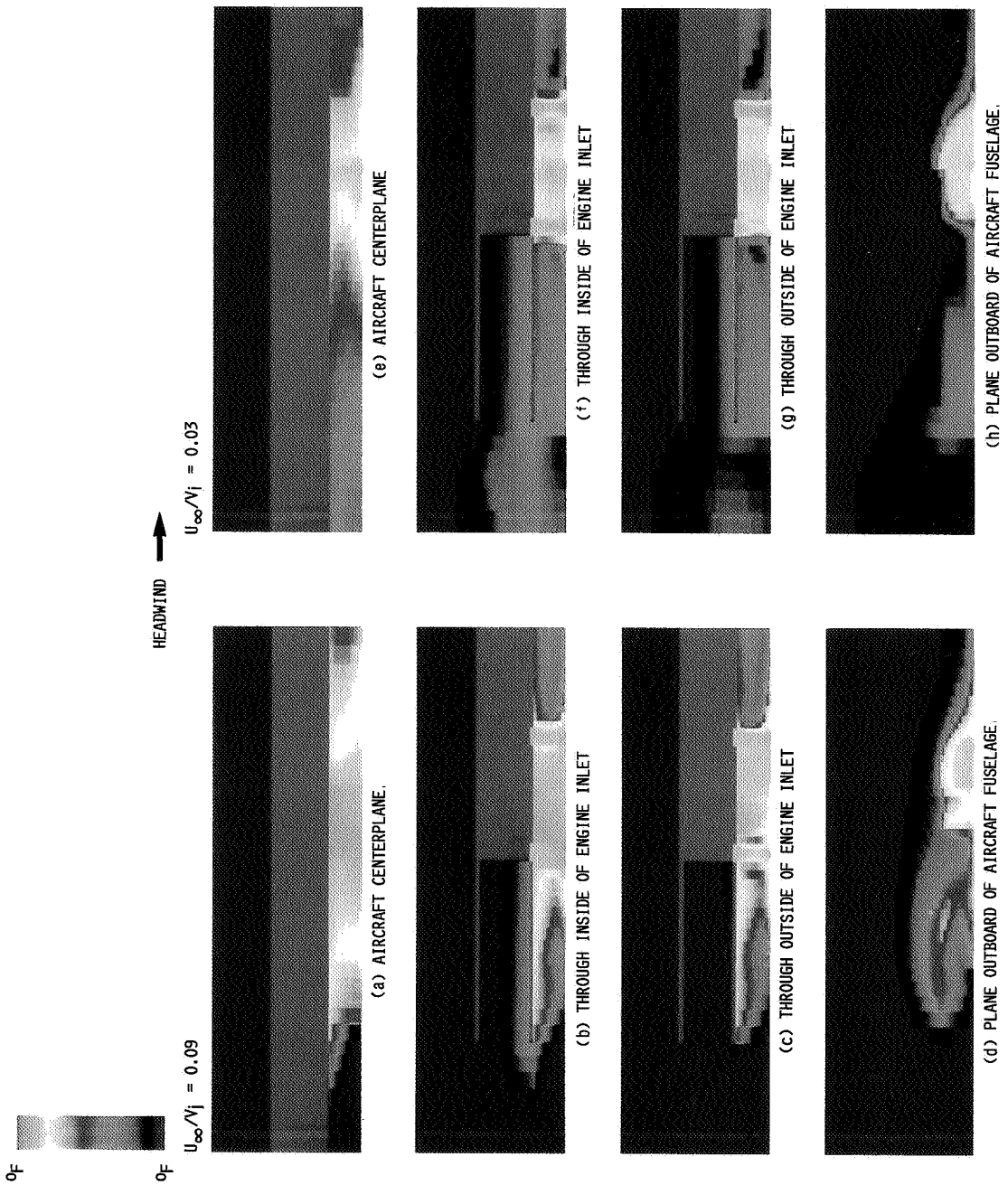

Fig 19 Temperature distributions in vertical planes for $H/D_j = 2$.

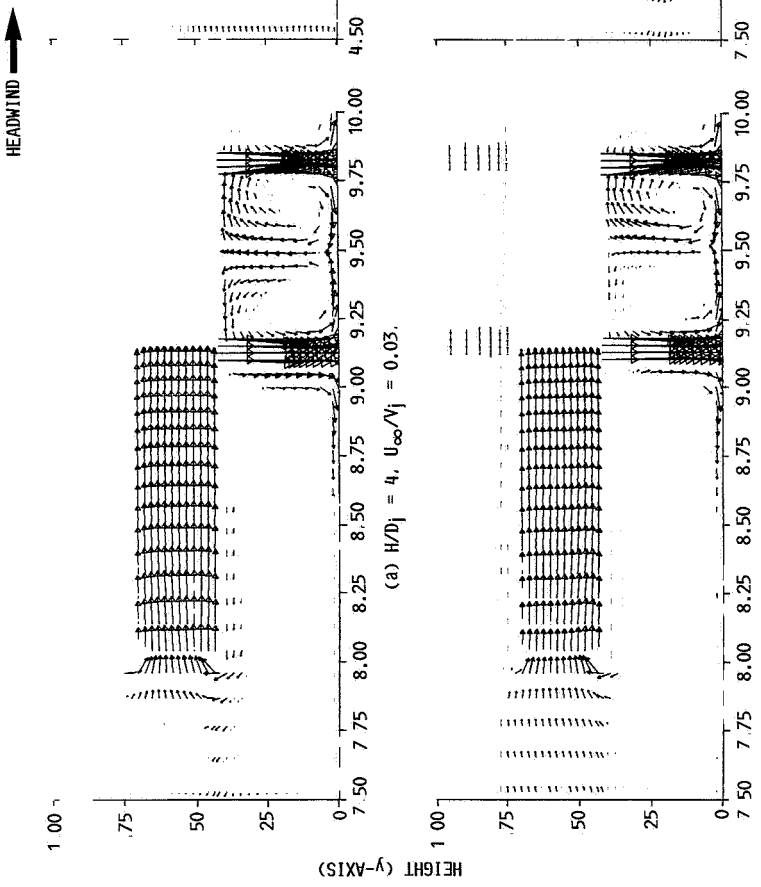

Fig. 20 Velocity vector distributions in vertical plane through engine inlet and lift jets.

ORIGINAL PAGE
COLOR PHOTOGRAPH

Fig 21 Comparison of temperature distributions in first axial (y-z) through engine inlet.

NASA
National Aeronautics and Space Administration

Report Documentation Page

1. Report No.	2. Government Accession No.	3. Recipient's Catalog No.
NASA TM-100895 AIAA-88-2888		

4. Title and Subtitle

A Numerical Study of the Hot Gas Environment Around a STOVL Aircraft in Ground Proximity

5. Report Date

6. Performing Organization Code

7 Author(s)

Thomas J VanOverbeke and James D. Holdeman

8. Performing Organization Report No.

E-4138

10. Work Unit No.

505-62-21

9. Performing Organization Name and Address

National Aeronautics and Space Administration
Lewis Research Center
Cleveland, Ohio 44135-3191

11 Contract or Grant No.

13. Type of Report and Period Covered

Technical Memorandum

12. Sponsoring Agency Name and Address

National Aeronautics and Space Administration
Washington, D.C 20546-0001

14. Sponsoring Agency Code

15. Supplementary Notes

Prepared for the 24th Joint Propulsion Conference cosponsored by the AIAA, ASME, SAE, and ASEE, Boston, Massachusetts, July 11-13, 1988.

16. Abstract

The development of Short Take-off Vertical Landing (STOVL) aircraft has historically been an empirical- and experience-based endeavor In this study, a 3-D turbulent flow CFD code was used to calculate the hot gas environment around a STOVL aircraft operating in ground proximity Preliminary calculations are reported herein for a typical STOVL aircraft configuration to identify key features of the flow field, and to demonstrate and assess the capability of current 3-D CFD codes to calculate the temperature of the gases ingested at the engine inlet as a function of flow and geometric conditions.

17 Key Words (Suggested by Author(s))	18. Distribution Statement
STOVL, Hot gas reingestion; Computational fluid dynamics; Modeling; Elliptic flow	Unclassified - Unlimited Subject Category 01

19. Security Classif. (of this report)	20. Security Classif. (of this page)	21. No of pages	22. Price*
Unclassified	Unclassified	27	A03

*For sale by the National Technical Information Service, Springfield, Virginia 22161